ACS ES&T Water

pubs.acs.org/estwater

Article

# Spectroscopic and Modeling Investigation of Sorption of Pb(II) to ZSM-5 Zeolites

Yunhui Zhang, Daniel S. Alessi,* Ning Chen, Mina Luo, Weiduo Hao, Md. Samrat Alam, Kurt O. Konhauser, Yong Sik Ok, and Abir Al-Tabbaa

Cite This: *ACS EST Water* 2021, 1, 108–116

Read Online

ACCESS | Metrics & More | Article Recommendations | Supporting Information

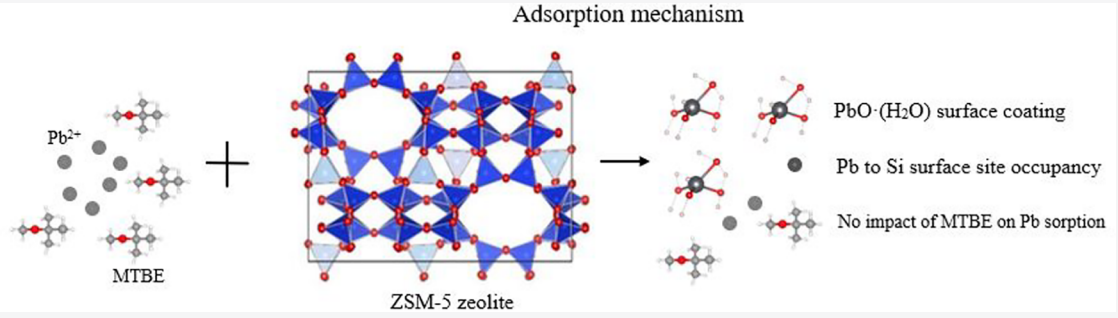


**ABSTRACT:** Methyl *tert*-butyl ether (MTBE) was used as a replacement for Pb in gasoline before it was found to be harmful, and for this reason, these two contaminants often coexist in groundwater at older fueling facilities. ZSM-5 is a well-characterized synthetic zeolite that shows promise in the removal of organic contaminants from water. While numerous studies have quantified the adsorption of metal to hydrophilic zeolites, few have investigated the mechanisms for adsorption to hydrophobic zeolites such as ZSM-5. In this study, batch adsorption tests and synchrotron-based extended X-ray absorption fine structure (EXAFS) analyses were conducted to investigate the adsorption of Pb to ZSM-5 in the presence and absence of MTBE. Batch adsorption studies showed that MTBE did not significantly impact Pb adsorption. EXAFS analyses revealed two Pb binding mechanisms: (1) precipitation as a $PbO{\cdot}(H_2O)$ type surface coating and (2) adsorption of Pb at Si surface sites. The $PbO{\cdot}(H_2O)$ type surface coating is more stable at pH 6 due to the formation of solid-phase hydroxide minerals, while the Pb to Si surface site occupancy is constrained by the availability of silanol sites on the surface. Our study provides an understanding of the mechanisms of precipitation and/or adsorption of Pb to hydrophobic zeolites and new insights into the synthesis and/or modification of zeolites to target the removal of co-contaminants from water and wastewater.

**KEYWORDS:** *clean water and sanitation, green and sustainable remediation, adsorbent, surface coating, advanced spectroscopic analysis*

## 1. INTRODUCTION

Heavy metals that are released into the environment are a major public health concern due to their toxic nature and persistence, and lead (Pb) is among the most common.[1−4] A wide range of remediation methods have been investigated to remove heavy metals from water and wastewater, including surface precipitation,[5] ion exchange,[6] electrochemical processes,[7] adsorption,[8,9] and a combination of these methods.[10] Of the methods described above, adsorption is considered to be an efficient and economic method of metal remediation, and zeolites are some of the most widely used and low-cost adsorbents.[11] Methyl *tert*-butyl ether (MTBE) is a gasoline additive that replaced Pb as an octane enhancer and oxygenate in 1979 in the United States and has since been banned by the U.S. Environmental Protection Agency due to groundwater contamination concerns.[12] However, it is still commonly used in many countries such as Mexico, Chile, and Venezuela.[13] Release of MTBE occurs during transport, delivery, and storage in underground and surface tanks, and for this reason, it often co-occurs with Pb and other potentially toxic heavy metals.[14] Despite this concern, few studies have been conducted to examine the effects of MTBE on the adsorption behavior of these metals.

Heavy metal removal by zeolites has generally been investigated by exploring adsorption kinetics, developing equilibrium isotherms, and determining the impact of various influencing factors such as pH, ionic strength, and co-contaminant interactions. While the adsorption of metals to zeolites is well-studied, less is known about the environments

Received: June 4, 2020
Revised: August 30, 2020
Accepted: September 2, 2020
Published: September 15, 2020

for binding of metals to the zeolite surface at an atomic level. This can be addressed with synchrotron-based X-ray absorption spectroscopy (XAS) investigations that can effectively identify the oxidation states and coordination environment of metal ions sorbed onto ion-exchanged materials, e.g., biochars,[15−17] clay minerals,[18] zeolites,[19,20] and metal oxides.[21,22] However, with respect to zeolites, most XAS studies of the adsorption of heavy metals focus on hydrophilic zeolites, such as clinoptilolite,[23,24] which are known to be excellent adsorbents of metal cations. By comparison, hydrophobic zeolites generally have a high adsorption capacity for organic compounds but inferior heavy metal adsorption capacities. Accordingly, few studies have determined the local coordination geometry of metals bound to these zeolites, including ZSM-5. For example, Ju et al.[25] found that $Pb^{2+}$ ion-exchanged ZSM-5 consisted of highly dispersed three-coordinate Pb(II) species with a Pb−O atomic distance of 2.3 Å. Bordiga et al.[26] revealed that the local environments of $Ag^{+}$ and $Cu^{2+}$ were similar in exchanged ZSM-5 with $Cu^{2+}$ surrounded by 2.5 ± 0.3 oxygen atoms at a metal−oxygen distance of 2.00 ± 0.02 Å and $Ag^{+}$ surrounded by 2.5 ± 0.4 oxygen atoms at a distance of 2.30 ± 0.03 Å. The different metal−oxygen distances were explained by the larger ionic radius of $Ag^{+}$, while the coordination numbers (CNs) were considered to be equal (2.5). Morra et al.[27] first resolved hyperfine interactions of $Zn^{2+}$ with a nearby Al nucleus with a Zn−Al distance of 2.88 Å in a $Zn^{2+}$-loaded ZSM-5. Shao et al.[28] found that Eu(III) bound to the ≡SOH sites of ZSM-5, and extended X-ray absorption fine structure (EXAFS) analysis indicated an Eu−O interatomic distance of 2.31 ± 0.01 Å with a CN of 7.7 and a residual factor of 0.045.

The concentrations of divalent metals such as Pb(II) may be increased in groundwater at contaminated sites, and these metals may form precipitates under modestly alkaline conditions.[29] Adsorption, ion exchange, and/or surface precipitation reactions may be active when using zeolites like ZSM-5 to treat contaminated groundwater, and understanding the mechanisms of removal and coordination of sorbed Pb ions at the zeolite surface is critical to making accurate estimates of sorbent efficacy. For this reason, ZSM-5 and Pb were chosen as a representative hydrophobic zeolite and heavy metal, respectively, to investigate their sorption characteristics in aqueous solution and explore the binding environment of Pb. The study aims (1) to provide the protonation constants and site densities of ZSM-5 surface functional groups using potentiometric titrations and a constant capacitance surface complexation model, (2) to describe the characteristics of sorption of Pb(II) to ZSM-5 in aqueous solution, (3) to evaluate the effects of solution pH and the coexistence of MTBE on the removal of Pb from solution, and (4) to explore the oxidation states and coordination environments of sorbed Pb using synchrotron-based EXAFS analysis.

## 2. MATERIALS AND METHODS

**2.1. Materials.** The hydrogen form of ZSM-5 was purchased from Acros Organics. It has a particle size of 2−8 μm, a surface area of 400 $m^2/g$, and a $SiO_2/Al_2O_3$ molar ratio of 469. Other detailed physicochemical properties can be found in our previous study.[30,31] The X-ray diffraction (XRD) pattern and SEM image can be found in Figures S1 and S2, respectively. Hydrochloric acid (HCl, 37%) and sodium hydroxide (NaOH) of ACS grade or higher were used to adjust the solution pH in the batch adsorption experiments.

**2.2. Potentiometric Titrations.** Potentiometric titrations were conducted to determine the concentrations and acidity constant ($K_a$) values of proton-active surface functional groups of the zeolite. Prior to a potentiometric titration, the pH electrode (Metrohm 905 Titrando) was calibrated using a set of three pH buffers and then placed in a covered sample cup containing a magnetic stir bar and dispensers for acid (0.1 M HCl) and base (0.1 M NaOH) titrants. Approximately 0.05 g of dry ZSM-5 powder was suspended in 50 mL of a 0.01 M $NaNO_3$ electrolyte solution. The sample containers were then sealed with Parafilm and purged with $N_2$ gas for 30 min prior to each titration and throughout the titration process to maintain a $CO_2$-free solution. A full titration consisted of a forward titration and backward titration: the forward titration (pH 3 to 11) was performed by adding small aliquots of 0.1 M NaOH, and the backward titration (pH 11 to 3) was conducted by adding small aliquots of 0.1 M HCl. Hysteresis was not observed when comparing forward and backward titrations, indicating that the sorbent was not damaged during the titration procedure and that proton adsorption was fully reversible. Additional information about the titration protocols can be found in our previous papers.[32,33]

**2.3. Pb(II) Adsorption Tests.** Batch Pb(II) adsorption experiments were conducted using 40 mg/L lead nitrate in a 1 M $NaNO_3$ solution to ensure a constant ionic strength. The typical pH of groundwater is in the range of 6−8.5, depending on the surrounding soil and rock types. Acidic groundwater also commonly exists in acidic mining discharge areas and in natural groundwater systems due to, for example, pyrite oxidation in acid sulfate soils.[34,35] Considering the wide range of groundwater pH, the experiments were carried out in increments of 1 pH unit, between pH 2 and 10, with a solid:liquid ratio of 1 g/L. The initial concentrations of $Pb^{2+}$ were 1, 5, 10, 20, 40, and 100 mg/L to determine the adsorption isotherm for ZSM-5. The effect of the existence of MTBE was evaluated by the addition of 100 mg/L MTBE. Control experiments were also carried out under identical conditions without the addition of ZSM-5. After being shaken for 24 h to ensure a stable pH and equilibrium adsorption of Pb, the supernatant was filtered through 0.20 μm nylon membranes (Millex HP). The filtered supernatants were analyzed for dissolved Pb concentrations at the University of Alberta Environmental Geochemistry Laboratory by inductively coupled plasma mass spectrometry (ICP-MS/MS; Agilent model 8800). All experiments were conducted in duplicate.

**2.4. X-ray Absorption Spectroscopy (XAS) Data Collection and Analysis.** XAS was utilized to investigate the oxidation states and coordination environments of Pb adsorbed to ZSM-5. Lead L3-edge EXAFS data were collected at the Hard X-ray Micro-Analysis (HXMA) beamline of the Canadian Light Source (CLS) in Saskatoon, Canada.[36] ZSM-5 samples from Pb adsorption experiments conducted at pH 4 and 6 were used for EXAFS analyses. During the measurements, the CLS storage ring was operated at 220 mA, and the beamline superconducting wiggler was run in a 2.2 T magnitude field. The beamline was configured in its focused mode with Rh mirrors (collimating and focusing mirrors) in the X-ray beam path. The X-ray beam photon energy was initially calibrated by a lead metallic foil provided by EXAFS Materials, and the same Pb foil was set at the downstream position of the sample, located between the second and third straight ion chamber detectors, making the in-step energy


https://dx.doi.org/10.1021/acsestwater.0c00010
ACS EST Water 2021, 1, 108−116

calibration available for each EXAFS scan. To decrease the high harmonic components in the incident X-ray beam, the second crystal of the monochromator Si(111) crystal was detuned by 50% at the end of the scan. EXAFS measurements were taken in transmission mode for the model compound lead oxide hydrate [$PbO\cdot(H_2O)$][37] and conducted in fluorescence mode for the Pb sample system using a 32-element Ge array detector. The Pb L3-edge data collection configuration for the full EXAFS experiment was (−200 to −30 eV; 10 eV/step, 2 s/point) for the pre-edge region, (−30 to 70 eV; 0.5 eV/step, 2 s/point) for X-ray absorption near-edge structure (XANES), and (70 eV to 14 $Å^{-1}$; 0.05 $Å^{-1}$/step, 2−10 s/point) for EXAFS. Following the standard procedure, the model compound $PbO\cdot(H_2O)$ was diluted using boron nitride (BN) powder to a concentration corresponding roughly to a XANES unit-edge jump. Data reduction and Feff 7-based[38] R space curve fitting were performed using the ATHENA software package[39] and WINXAS version 2.3,[40] respectively. XANES theoretical modeling was performed using the code FDMNES.[41]

## 3. RESULTS

**3.1. Protonation Model of ZSM-5.** Potentiometric titrations were conducted to determine the proton buffering capacity of ZSM-5. The titration curves were modeled using a constant capacitance model (CCM) to determine the proton binding constants and site concentrations of surface functional groups. The fitting results are shown in Figure S3 and Table 1.

**Table 1. Calculated Parameters from the Protonation Model of Titration Data of ZSM-5[a]**

| | $\equiv L_1^-$ | $\equiv L_2^-$ | $V_Y$ (variance) |
|---|---|---|---|
| $pK_a$ | 9.09 | 6.07 | 3.09 |
| site density (mol/g) | $3.25 \times 10^{-4}$ | $7.47 \times 10^{-5}$ | |
| capacitance ($F/m^2$) | 5 | | |

[a] $\equiv L_1^-$ and $\equiv L_2^-$ are surface functional groups.

Titration data were modeled using the software package FITEQL 3.2,[42] which uses a least-squares error approach to solve for a discrete number of proton-active sites and their corresponding site concentrations.[43] Several fitting approaches were attempted, including invoking between one and four proton active sites, and considering the presence of an amphoteric surface site with, and without, an additional monoprotic site. A two-site protonation model best simulated the experimental data, according to the following equations:

$$\equiv L_1H \leftrightarrow \equiv L_1^- + H^+ \quad (1)$$

$$K_{L_1H} = \frac{[\equiv L_1^-]\alpha_{H^+}}{[\equiv L_1H]} \quad (2)$$

$$\equiv L_2H \leftrightarrow \equiv L_2^- + H^+ \quad (3)$$

$$K_{L_2H} = \frac{[\equiv L_2^-]\alpha_{H^+}}{[\equiv L_2H]} \quad (4)$$

The $L_2$ site has a density of $7.47 \times 10^{-5}$ mol/g. This is similar in magnitude to that of basal sites on previously studied clays,[32,33] suggesting that $L_2$ represents basal sites, which can be either aluminum hydroxide (≡Al−OH) or silanol (≡Si−OH) sites at the zeolite surface. The density of $L_1$ sites ($3.25 \times 10^{-4}$ mol/g) is higher than for $L_2$, and using clays again as a comparison, it is likely that $L_1$ represents ion exchange sites (generated by isomorphic substitution) because they generally have a site density that if higher than that of basal sites.[32,33] With regard to ZSM-5, there is limited isomorphic substitution of $Si^{4+}$ by $Al^{3+}$ as compared to that in clay minerals and another ZSM-5 that has a lower Si:Al ratio;[28] however, the 10-membered ring in the ZSM-5 structure provides sites for exchange reactions with ions in aqueous solution. Thus, we hypothesize that $L_1$ represents ion exchange sites in the Si tetrahedron ring structure of zeolites instead of isomorphic substitution, which is consistent with the EXAFS investigation that follows.

**3.2. Sorption of Pb to ZSM-5.** *3.2.1. Sorption Isotherms.* Equilibrium sorption of heavy metals, including Pb, onto zeolites is often shown to occur within 12 h.[44,45] To determine the sorption capacity of ZSM-5 for Pb, batch sorption equilibrium tests were conducted with a series of initial Pb concentrations from 1 to 100 mg/L at pH 4 and 6. These concentrations were chosen on the basis of estimates of sorption capacity from trial tests. As shown in Figure S4 and Table 2, the Langmuir and Freundlich models adequately describe the experimental sorption data ($R^2 > 0.95$, and $p < 0.01$). The Akaike's information criterion (AIC) values were further calculated as a quality control for these two models. The sorption of Pb to ZSM-5 was best fit by the Langmuir model at pH 4 and 6 as shown by the highest $R^2$ values and the lowest AIC values, and sorption was favorable ($0 < R_L < 1$). The value of $1/n$ from the Freundlich model is close to 1, indicating homogeneous binding sites on the surface of ZSM-5.

**Table 2. Isotherm Model Parameters for Sorption of Pb to ZSM-5 at pH 4 and 6**

| model | parameter | pH 4 | pH 6 |
|---|---|---|---|
| Langmuir model | $Q_0$ (mg/g) | 14.39 ± 5.83 | 46.34 ± 6.25 |
| | $b$ (L/mg) | 0.009 ± 0.006 | 0.016 ± 0.004 |
| | $R_L$ | 0.991 | 0.984 |
| | AIC | 20.04 | 25.74 |
| | $p$ | 0.002 | $2.05 \times 10^{-4}$ |
| | $R^2$ | 0.967 | 0.993 |
| Freundlich model | $K_F$ (mg/g) | 0.16 ± 0.10 | 1.12 ± 0.25 |
| | $1/n$ | 0.81 | 0.72 |
| | AIC | 21.64 | 27.10 |
| | $p$ | 0.003 | $3.07 \times 10^{-4}$ |
| | $R^2$ | 0.955 | 0.990 |

As shown in Table 2, the sorption capacity of ZSM-5 at pH 6 was 46.34 mg/g, triple that at pH 4 (14.39 mg/g). The Pb speciation diagram (Figure S5) showed that lead hydroxide, $PbO\cdot(H_2O)$, was the major precipitate, whereas lead carbonate does not form even when solution equilibrium with atmospheric $CO_2$ is considered. Therefore, the higher sorption capacity at pH 6 was mainly due to the precipitation of Pb(II) to form a hydroxide surface coating on the zeolite. The results of the control experiments also revealed that Pb(II) began to precipitate from pH 5.5 (Figure S6), indicating the formation of lead hydroxide precipitants onto the surface of ZSM-5 or into the solution at pH 6. In addition, the removal of heavy metals, including Pb(II), from aqueous solution is known to be greatly influenced by the surface chemistry and the number of adsorption sites of zeolites.[46,47]


https://dx.doi.org/10.1021/acsestwater.0c00010
ACS EST Water 2021, 1, 108−116

ZSM-5 has a relatively low Pb sorption capacity as compared with those of many other adsorbents, such as activated carbon (AC), clay, biochar, and other zeolites (see Table 3), especially

**Table 3. Comparison of Sorption Capacities of Pb onto Different Adsorbents**

| sorbent | sorption capacity (mg/g) | pH | ref |
|---|---|---|---|
| peanut husk AC | 113.96 | 6 | 48 |
| pine cone AC | 27.53 | 5.2 | 49 |
| montmorillonite-illite type clay | 52 | 4 | 50 |
| sludge biochar | 30.9 | 5 | 51 |
| sesame straw biochar | 102 | 7 | 52 |
| buffalo weed biochar | 333.33 | 5 | 53 |
| natural zeolite tuff | 78.6 | 5 | 54 |
| clinoptilolite | 80.93 | 4.5 | 55 |
| clinoptilolite | 117.64 | 4 | 56 |
| clinoptilolite | 108.69 | 6 | 56 |
| ZSM-5 | 20.1 | 3 | 57 |
| ZSM-5 | 14.39 | 4 | this study |
| ZSM-5 | 46.34 | 6 | this study |

at pH 4 where Pb(II) does not precipitate as a lead hydroxide. The unbalanced substitution of $Si^{4+}$ with $Al^{3+}$ in the crystalline lattice of zeolite can lead to a net negative charge, resulting in an increase in the number of free cations that can exchange with metal ions, including $Pb^{2+}$, in the adsorption process. ZSM-5 has a high Si:Al ratio and, therefore, few free cations that can exchange with $Pb^{2+}$, leading to its low adsorption capacity for Pb(II).

*3.2.2. Effect of pH and the Presence of MTBE.* The effect of solution pH on sorption of Pb(II) to ZSM-5 in the pH range of 2−10 with and without the presence of MTBE is shown in Figure 1. Adsorbed Pb(II) remains below 4.5% between pH 2

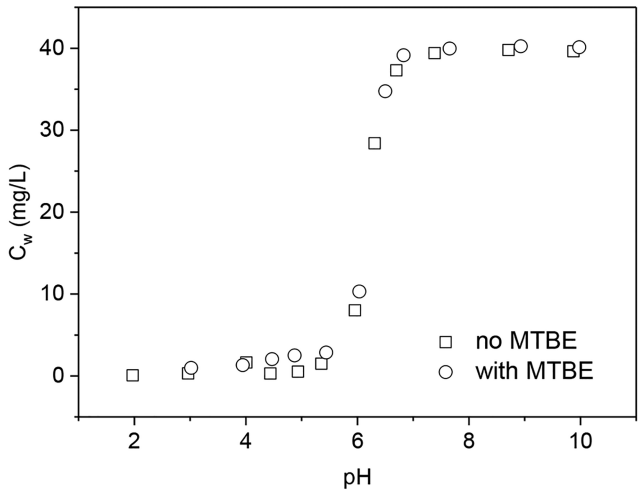


**Figure 1.** pH-edge plots of sorption of Pb to ZSM-5 with and without the existence of MTBE.

and 5.5, increases rapidly to nearly 100% with increased pH's from 5.5 to 7.5, and then stays constant until the pH reaches 10. Pb(II) begins to precipitate from pH 6.5.

The presence of MTBE had a negligible effect on the sorption of Pb to ZSM-5 at all pH values (Figure 1). According to the high adsorption capacity (53.55 mg/g) of ZSM-5 for MTBE obtained in our previous study,[58] both Pb and MTBE were added to the solution in excess during co-sorption experiments. In this way, the adsorption reached saturation for both Pb and MTBE on the surface of ZSM-5. We observed that MTBE tends to enter the pores of ZSM-5,[30] while Pb(II) is likely adsorbed by ion exchange and surface precipitation. Therefore, the sorption of Pb and MTBE is not competitive, and the coexistence of MTBE has a negligible effect on the sorption of Pb to ZSM-5 under the conditions of this study.

**3.3. EXAFS Characterization.** M-1 and M-2 are EXAFS structural models developed to represent the $PbO{\cdot}(H_2O)$ type surface coating and Pb coordination at a Si-centered site, respectively, with details shown in the Supporting Information. EXAFS characterization revealed that M-1 type (Figure S7) and M-2 type (Figure S8) modes of Pb surface speciation coexist at pH 4 and 6. Therefore, an M-3 model was developed to combine the M-1 and M-2 models, and then M-3-based theoretical scattering amplitudes and phases were calculated using FEFF 7.02[38] to guide the R space curve fitting. The experimental data from the pH 6 sample were compared with the FEFF modeling in both R space (Figure S9a) and k space (Figure S9b). Two experimentally resolved data trends, "A" and "B", can be observed in Figure S10 and Figure 2. The

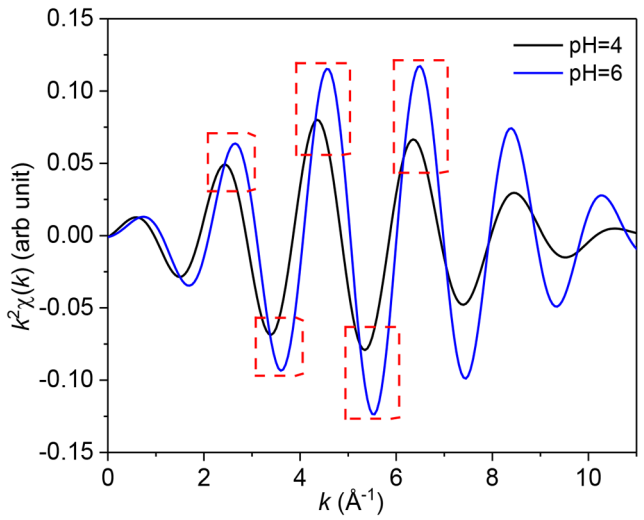


**Figure 2.** Backward FT-filtered $k^2\chi(k)$ ("sine" window function, FT window from 1.0 to 2.2 Å) at pH 4 and 6.

negative correlation of trend "A" and pH can be attributed to structural compression of the $PbO{\cdot}(H_2O)$ surface coating, while the positive correlation for trend "B" can be induced by the development of $PbO{\cdot}(H_2O)$ particles. This is consistent with the M-3-based R space curve fitting results listed in Table 5.

As shown in Table 5, paths 1−4 are the backscattering covered by the M-1 submodel and path 5 corresponds to the M-2 submodel. The fitted values of the interatomic distance ($R$) for the pH 4 sample closely match the distance for the corresponding path predicted by the M-3 model, indicating the existence of the precursor of $PbO{\cdot}(H_2O)$. Fitting reveals an overall consistency in the CN throughout all fitted paths between the pH 6 sample and submodel M-1, further supporting the existence of $PbO{\cdot}(H_2O)$ at pH 6. In addition, the fitted $R$ for the Pb−O1 path for the pH 6 sample of 2.28 Å is consistent with the 2.30 Å distance fitted by Ju et al.[25] in a


https://dx.doi.org/10.1021/acsestwater.0c00010
ACS EST Water 2021, 1, 108−116

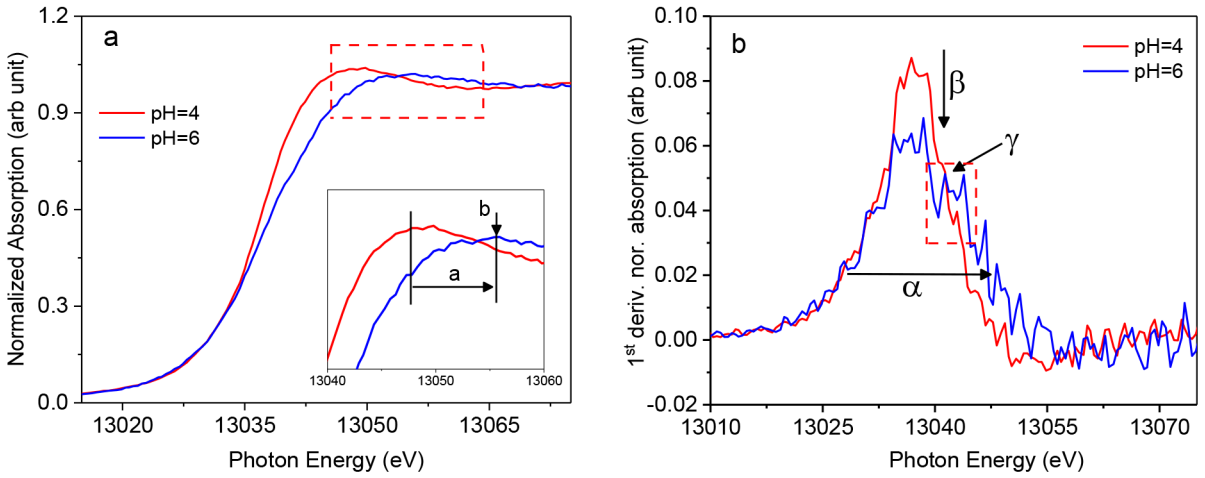


**Figure 3.** (a) XANES spectra and (b) their corresponding first derivatives for the Pb bearing ZSM-5 sample systems.

**Table 4. Correlation between XAS Data Rrends and pH Values**

| XAS | data trend | XAS feature details | correlation vs pH | |
|---|---|---|---|---|
| EXAFS | A | $k^2\chi(k)$ oscillation peak drifting | negative | Figure S10, Figure 3, and Table 5 |
| | B | $k^2\chi(k)$ oscillation amplitude changing | positive | Figure S10, Figure 3, and Table 5 |
| XANES | a | whiteline peak position energy drifting | positive | Figures S10 and S11a,c |
| | b | whiteline peak amplitude changing | negative | Figures S10 and S11a,c |
| | $\alpha$ | line width of the first-derivative peak of XANES spectra | positive | Figure 3 and Figure S11b,d |
| | $\beta$ | amplitude of the first-derivative peak of XANES spectra | negative | Figure 3 and Figure S11b,1d |
| | $\gamma$ | shoulder peak feature experimentally clearly resolved only at pH 6 | | Figure 3 and Figures S11d and S13 |

Pb-ZSM-5 system. The fitted CN (2.5) of this scattering path is ~3, suggesting a 3-fold O coordination,[59] consistent with the triangular configuration of the oxygen base of the distorted $PbO_4$ tetrahedron of $PbO{\cdot}(H_2O)$ [M-1 (Figure S7a)]. Although this triangular oxygen configuration has been previously reported,[59] the Pb−$O_2$ scattering (path 2 in this study) is novel. The $PbO_4$ tetrahedron and the further $PbO{\cdot}(H_2O)$ type surface precipitation were first identified on the surface of the ZSM-5 system during data analysis and fitting conducted in this study.

The fitted Pb−Si interatomic distances (3.05 and 3.07 Å, respectively) for the two samples match the corresponding average Si−Si path distance predicted by the crystallography of ZSM-5 (3.07 Å), indicating Pb occupancy at the Si site of ZSM-5 of the M-2 type. In addition, the reported CN and R results (Table 5) for the Pb−Si scattering observed in the two samples are also consistent with previous work by Um and Papelis,[60] who studied a $Pb^{2+}$/zeolitized tuffs system at pH 7.16 (CN = 1.0, and $R$ = 3.09 Å). However, the reported $R$ values for the Pb−Si scattering path in this study are shorter than those reported for sorption of $Pb^{2+}$ to amorphous silica ($R$ = 3.40−3.44 Å with different ionic strengths).[61] This is reasonable due to the fact that the $PbO_4$ tetrahedron site occupancy is constrained by the ZSM-5 surface structure, which is significantly different from that of amorphous silica. The impact of ionic strength on sorption of Pb to ZSM-5 will be tested in future studies.

**3.4. XANES Characterization.** Four systematic changes in the XANES spectra occurred from pH 4 to 6, as shown in Figure 3 and Table 4. On the basis of the EXAFS results described above, XANES theoretical modeling was used to address these four experimentally resolved XANES data trends ("a", "b", "$\alpha$", and "$\beta$"), while the "$\gamma$" feature is uniquely resolved at pH 6. Three structural systems, 1−3, were developed for this purpose (details can be found in the Supporting Information). The theoretical modeling based on structural system 1 aims to simulate the XANES features, which characterize the structural compression process for hydrated $PbO_4$ from pH 4 to 6. The modeled XANES system and the corresponding first-derivative XANES system reproduce the experimentally resolved data trends "a" and "b" (Figure S11a) and "$\alpha$" and "$\beta$" (Figure S11b), respectively. In addition to trends "a" and "b" (Figure S11c) and trends "$\alpha$" and "$\beta$" (Figure S11d), the "$\gamma$" feature (Figure S11d) has further been reproduced through system 2-based modeling. To further verify this observation, XANES theoretical modeling was performed on the basis of structural system 3 (Figure S12). The modeling indicates that "$\gamma$" begins to clearly resolve at the cluster $R$ of 4.0 Å (Figures S12b and S13) and reaches its peak amplitude at $R$ values of 4.0−5.0 Å (Figures S12c,2d and S13), which is consistent with the modeling results based on system 2.

## 4. DISCUSSION

The batch adsorption results indicated that the sorption of Pb to ZSM-5 was best fit by the Langmuir model. Being a hydrophobic zeolite, ZSM-5 has a relatively low sorption capacity for Pb (46.34 mg/g at pH 6 and 14.39 mg/g at pH 4) compared with other sorbents, such as hydrophilic zeolites, activated carbon, and biochar (Table 3). Sorption increased with an increased solution pH in the range of 2−10, mainly attributed to the precipitation of $Pb^{2+}$ to form lead hydroxide. However, the presence of MTBE (≤100 mg/L) had a negligible effect on the removal of Pb from solution, likely due to the differing sorption mechanisms of Pb and MTBE.


https://dx.doi.org/10.1021/acsestwater.0c00010
ACS EST Water 2021, 1, 108−116

Table 5. M-3-Based R Space Curve Fitting Results[a]

| | M-3 model | | | pH 4 | | | pH 6 | | |
|---|---|---|---|---|---|---|---|---|---|
| path (submodel) | path | CN | $R$ (Å) | CN | $R$ (Å) | $\sigma^2$ (Å$^2$) | CN | $R$ (Å) | $\sigma^2$ (Å$^2$) |
| 1 (M-1) | Pb−O1 | 3 | 2.32 | 1.8 | 2.35 | 0.0049 | 2.5 | 2.28 | 0.0050 |
| 2 (M-1) | Pb−O2 | 1 | 2.57 | 1.1 | 2.58 | 0.0049 | 1.1 | 2.52 | 0.0050 |
| 3 (M-1) | Pb−Pb1 | 2 | 3.98 | 1.0 | 3.71 | 0.0068 | 2.4 | 3.71 | 0.0068 |
| 4 (M-1) | Pb−Pb2 | 4 | 4.14 | 1.0 | 4.00 | 0.0100 | 3.5 | 4.00 | 0.0100 |
| 5 (M-2) | Pb−Si | 2 | 3.07 | 0.7 | 3.05 | 0.0068 | 1.1 | 3.07 | 0.0068 |

[a]Fitted $\Delta E_0$ values of −2.4 and −1.2 eV for pH 4 and 6, respectively.

The mechanisms of binding of Pb to ZSM-5 were investigated by synchrotron-based EXAFS analysis. EXAFS R space curve fitting reveals that the precursor of PbO·($H_2O$) particles forms at pH 4 due to the fact that both Pb−Pb1 and Pb−Pb2 can be clearly identified (Table 5 and Figure S7). The estimated CNs increased from undercoordinated (CN = 1.8, 1.0, and 1.0) at pH 4 to full coordination (CN = 2.5, 2.4, and 3.5) at pH 6 for the Pb−O1, Pb−Pb1, and Pb−Pb2 paths, respectively, closely matching the M-3 model (CN = 3, 2, and 4) in Table 5. This revealed a developmental process from the precursor of the PbO·($H_2O$) type at pH 4 to fully developed PbO·($H_2O$) particles at pH 6. Specifically, the backscattering from nearest neighbor coordinations will be experienced progressively by the center absorbing atom Pb, as recorded in the R space by EXAFS FT data (e.g., Figure S3b). With a decrease in the size of surface-precipitated PbO·($H_2O$) particles, more Pb atoms are exposed on the particle surface and experience the surface effect, i.e., a decrease in CN and changes in bond distances for corresponding scattering paths. This phenomenon between samples [pH 4 vs pH 6 (Table 5)] was observed and revealed corresponding changes in CN and $R$ for different nearest neighbor scattering paths. This experimentally revealed trend is attributed to the increasing particle size of PbO·($H_2O$) from pH 4 to 6.

In addition, a compression process of the PbO·($H_2O$) structural framework was characterized by a universal shortening effect from pH 4 to 6 for all paths of model M-3. This effect may be induced by the PbO·($H_2O$) surface coating process. When the PbO·($H_2O$) precursor developed initially at pH 4, the PbO·($H_2O$) particles may not completely fit the surface structure of ZSM-5. Therefore, these PbO·($H_2O$) particles retained the Pb local structural environment that is close to that of the undistorted PbO·($H_2O$) structure. During the coating process on the ZSM-5 surface, adjustment needs to occur in the Pb local structural environment to enable PbO·($H_2O$) particles to fit into the ZSM-5 surface structure. In view of the EXAFS results, this structural adjustment is characterized as an overall compression of the Pb local structural environment for those corresponding scattering paths (Table 5). Considering that this local structural adjustment should lead to a relatively lower-energy status of PbO·($H_2O$), Pb anchored through a PbO·($H_2O$) surface coating may be more stable at pH 6 than at pH 4.

EXAFS R space curve fitting identified Pb−Si single-path scattering, indicating the presence of Pb occupancy at the Si sites of ZSM-5 from pH 4 to 6. The fitted CN values (0.7 and 1.1 at pH 4 and 6, respectively) listed in Table 5 are close to 1, indicating that the Pb occupancy is likely located at the cleaved $SiO_4$ rings. As the cleaving of $SiO_4$ rings most likely occurs on the surface of ZSM-5 particles, leaving empty Si tetrahedron sites available for Pb uptake, the Pb to Si site occupancy can be expected to occur on the ZSM-5 surface sites rather than through a bulk type of occupancy. Therefore, ZSM-5 may have a relatively low adsorption capacity of the M-2 type toward Pb due to a limitation in the available number of $SiO_4$ rings on the ZSM-5 surface. The slight increase in CN in relation to the Pb−Si scattering from pH 4 to 6 suggests that the Pb occupancy at Si sites may be more stable or better defined at pH 6 than at pH 4. The fitted Pb−Si interatomic distance (Table 5) is between 3.05 and 3.07 Å, consistent with the average Si−Si distance of the three types of Si rings in the ZSM-5 framework (Table 4). This observation reveals that the scale of the local structural perturbation induced by Pb site occupancy is smaller than the EXAFS resolution. Therefore, the exact location of the Pb occupancy on the Si rings (Figure S7b−d) of ZSM-5 cannot be identified using the current EXAFS data. In addition, EXAFS reveals a tetrahedron Pb site occupancy. Pb directly reacted with O to develop its first-shell coordination. The Pb first shell is coordinated to O, which is further coordinated to the Pb outer shell Si from the $SiO_4$ ring of the ZSM-5 structure; thus, those O atoms are shared by both Pb and Si. The outer shell Si impacts the local coordination environment of Pb through those shared O atoms. The crystal defects may also impact the adsorption of lead ions to ZSM-5, and a systematic study of their impacts on adsorption properties would be valuable.

The XANES results were consistent with the observations gathered from the EXAFS data. Through systematic modeling based on structural systems 1 and 2, the experimentally resolved data trends "a", "b", "$\alpha$", and "$\beta$" were addressed by the compression effect of the Pb local structural framework of PbO·($H_2O$) up to the second-shell Pb−Pb coordination. In addition, the modeling based on systems 2 and 3 further verified that the XANES feature "$\gamma$" was induced by Pb−Pb scattering from the first-shell Pb−Pb and further outer shell Pb−Pb coordination. Therefore, "$\gamma$" is the fingerprint feature of the Pb−Pb coordination of the PbO·($H_2O$) type. It should be noted that the Pb−Si site occupancy is likely to be a point of nucleation of PbO·($H_2O$) particles.

## 5. ENVIRONMENTAL IMPLICATIONS

This study provides mechanistic insights into the binding of Pb(II) to ZSM-5 using synchrotron-based investigations and adsorption modeling and investigates the effects of MTBE on the removal of Pb(II) from solution by ZSM-5. We found that MTBE has a negligible effect on the sorption of Pb(II) to ZSM-5, suggesting that the simultaneous treatment of these commonly occurring co-contaminants is feasible using the zeolite. The EXAFS analyses reveal that Pb to Si surface site occupancy (adsorption) and the formation of PbO·($H_2O$) type surface coatings (precipitation) are the two main mechanisms of binding Pb(II) to ZSM-5. The PbO·($H_2O$) type of surface coating played the more important role at pH 6, which explains


https://dx.doi.org/10.1021/acsestwater.0c00010
ACS EST Water 2021, 1, 108−116

why the amount of Pb removal from solution increased with an increased solution pH. The low Pb adsorption capacity at pH 4 can be explained by the limited availability of $SiO_4$ rings on the ZSM-5 surface, especially incomplete $SiO_4$ rings, which constrained Pb to Si surface site occupancy due to its activity in Pb uptake. Without the development of a surface treatment that can increase the concentration of Si sites, Pb coordination at Si surface sites plays a subordinate role in Pb uptake versus the development of $PbO\cdot(H_2O)$ type surface coatings. Therefore, future studies should investigate the development of modification or synthesis methods to increase the number of incomplete $SiO_4$ rings on the ZSM-5 surface and expose these sites to Pb, which will improve its adsorption performance for Pb(II) and other heavy metal cations. More generally, this study also offers novel insights into the modification and synthesis of other zeolites to target metal ions for water treatment purposes.

## ■ ASSOCIATED CONTENT

### Supporting Information

The Supporting Information is available free of charge at https://pubs.acs.org/doi/10.1021/acsestwater.0c00010.

Descriptions of the structural models (M-1−M-3) and structural systems (1−3) developed for EXAFS and XANES analyses, respectively; XRD, SEM, and titration results for ZSM-5 zeolites; adsorption isotherm fitting for Pb adsorption on ZSM-5; speciation diagram for the Pb−ZSM-5 adsorption system; effect of pH on Pb adsorption; schematic diagrams of the ZSM-5 structural framework, M-1 model, M-2 model, and systems 1−3; Si−Si distances of the three types of $SiO_4$ rings; R space curve fitting result of the pH 6 sample; comparison of raw $k^2\chi(k)$ data between the pH 4 sample and the pH 6 sample; theoretical XANES system and the corresponding first-derivative XANES system based on structural systems 1−3; comparison of XANES, $k^2\chi(k)$, and the backward FT-filtered $k^2\chi(k)$ results between the $PbO\cdot(H_2O)$ model and the pH 6 sample; comparison between experimental data of $PbO\cdot(H_2O)$ and the crystallography-based Feff modeling in $k^2\chi(k)$; and magnitude of FT for $k^2\chi(k)$, backward FT filtered in $k^2\chi(k)$ for first-shell Pb−O coordination (PDF)

## ■ AUTHOR INFORMATION


### Corresponding Author

**Daniel S. Alessi** − *Department of Earth and Atmospheric Sciences, University of Alberta, Edmonton T6G 2E3, Canada;* orcid.org/0000-0002-8360-8251; Phone: +1-780-492-8019; Email: alessi@ualberta.ca

### Authors

**Yunhui Zhang** − *Department of Engineering, University of Cambridge, Cambridge CB2 1PZ, United Kingdom; Department of Earth and Atmospheric Sciences, University of Alberta, Edmonton T6G 2E3, Canada;* orcid.org/0000-0001-7134-1951

**Ning Chen** − *Canadian Light Source Inc., University of Saskatchewan, Saskatoon, Saskatchewan S7N 0X4, Canada;* orcid.org/0000-0002-1269-6119

**Mina Luo** − *College of Chemistry and Chemical Engineering, Southwest Petroleum University, Chengdu 610500, China*

**Weiduo Hao** − *Department of Earth and Atmospheric Sciences, University of Alberta, Edmonton T6G 2E3, Canada;* orcid.org/0000-0002-0486-424X

**Md. Samrat Alam** − *Department of Earth and Atmospheric Sciences, University of Alberta, Edmonton T6G 2E3, Canada; Department of Earth Sciences, University of Toronto, Toronto, ON M5S 3B1, Canada*

**Kurt O. Konhauser** − *Department of Earth and Atmospheric Sciences, University of Alberta, Edmonton T6G 2E3, Canada*

**Yong Sik Ok** − *Korea Biochar Research Center, APRU Sustainable Waste Management and Division of Environmental Science and Ecological Engineering, Korea University, Seoul 02841, Korea;* orcid.org/0000-0003-3401-0912

**Abir Al-Tabbaa** − *Department of Engineering, University of Cambridge, Cambridge CB2 1PZ, United Kingdom*

Complete contact information is available at: https://pubs.acs.org/10.1021/acsestwater.0c00010


### Notes

The authors declare no competing financial interest.

## ■ ACKNOWLEDGMENTS

Y.Z. thanks the China Scholarship Council (CSC) for providing a Ph.D. studentship. Research expenses were supported by Natural Sciences and Engineering Research Council of Canada (NSERC) Discovery grants to D.S.A. (RGPIN-04134) and K.O.K. (RGPIN-165831).

## ■ REFERENCES


(1) Zhang, Y.; Hou, D.; O'Connor, D.; Shen, Z.; Shi, P.; Ok, Y. S.; Tsang, D. C. W.; Wen, Y.; Luo, M. Lead Contamination in Chinese Surface Soils: Source Identification, Spatial-Temporal Distribution and Associated Health Risks. *Crit. Rev. Environ. Sci. Technol.* **2019**, *49*, 1386−1423.

(2) Zhang, Y.; O'Connor, D.; Xu, W.; Hou, D. Blood Lead Levels among Chinese Children: The Shifting Influence of Industry, Traffic, and e-Waste over Three Decades. *Environ. Int.* **2020**, *135*, 105379.

(3) Ahmad, M.; Soo Lee, S.; Yang, J. E.; Ro, H. M.; Han Lee, Y.; Sik Ok, Y. Effects of Soil Dilution and Amendments (Mussel Shell, Cow Bone, and Biochar) on Pb Availability and Phytotoxicity in Military Shooting Range Soil. *Ecotoxicol. Environ. Saf.* **2012**, *79*, 225.

(4) Tian, D.; Li, Z.; O'Connor, D.; Shen, Z. The Need to Prioritize Sustainable Phosphate-based Fertilizers. *Soil Use Manage.* **2020**, *36*, 351−354.

(5) Zhang, Y.; Wu, L.; Huang, P.; Shen, Q.; Sun, Z. Determination and Application of the Solubility Product of Metal Xanthate in Mineral Flotation and Heavy Metal Removal in Wastewater Treatment. *Miner. Eng.* **2018**, *127*, 67−73.

(6) Kulkarni, V. V.; Golder, A. K.; Ghosh, P. K. Synthesis and Characterization of Carboxylic Cation Exchange Bio-Resin for Heavy Metal Remediation. *J. Hazard. Mater.* **2018**, *341*, 207.

(7) Tao, H. C.; Lei, T.; Shi, G.; Sun, X. N.; Wei, X. Y.; Zhang, L. J.; Wu, W. M. Removal of Heavy Metals from Fly Ash Leachate Using Combined Bioelectrochemical Systems and Electrolysis. *J. Hazard. Mater.* **2014**, *264*, 1.

(8) Hao, W.; Pudasainee, D.; Gupta, R.; Kashiwabara, T.; Alessi, D. S.; Konhauser, K. O. Effect of Acidic Conditions on Surface Properties and Metal Binding Capacity of Clay Minerals. *ACS Earth Sp. Chem.* **2019**, *3* (11), 2421−2429.

(9) Shen, Z.; Zhang, Y.; Jin, F.; Alessi, D. S.; Zhang, Y.; Wang, F.; McMillan, O.; Al-Tabbaa, A. Comparison of Nickel Adsorption on Biochars Produced from Mixed Softwood and Miscanthus Straw. *Environ. Sci. Pollut. Res.* **2018**, *25* (15), 14626−14635.

(10) Abou-Shady, A.; Peng, C.; Bi, J.; Xu, H.; Almeria O, J. Recovery of Pb (II) and Removal of NO 3- from Aqueous Solutions Using

Integrated Electrodialysis, Electrolysis, and Adsorption Process. *Desalination* **2012**, *286*, 304.
(11) Babel, S.; Kurniawan, T. A. Low-Cost Adsorbents for Heavy Metals Uptake from Contaminated Water: A Review. *J. Hazard. Mater.* **2003**, *97* (1−3), 219−243.
(12) World Health Organization. Methyl Tertiary-Butyl Ether (MTBE) in Drinkingwater, Background Document for Development of WHO Guidelines for Drinking-Water Quality. 2005.
(13) U.S. EIA (Energy Information Administration). The United States continues to export MTBE, mainly to Mexico, Chile, and Venezuela.
(14) Fernandes, V. C.; Albergaria, J. T.; Oliva-Teles, T.; Delerue-Matos, C.; De Marco, P. Dual Augmentation for Aerobic Bioremediation of MTBE and TCE Pollution in Heavy Metal-Contaminated Soil. *Biodegradation* **2009**, *20* (3), 375−382.
(15) Alam, M. S.; Gorman-Lewis, D.; Chen, N.; Flynn, S. L.; Ok, Y. S.; Konhauser, K. O.; Alessi, D. S. Thermodynamic Analysis of Nickel(II) and Zinc(II) Adsorption to Biochar. *Environ. Sci. Technol.* **2018**, *52*, 6246.
(16) Chen, N.; Alam, M. S.; Alessi, D. S. XAS Characterization of Nano-Chromite Particles Precipitated on Magnetite-Biochar Composites. *Radiat. Phys. Chem.* **2020**, *175*, 108544.
(17) Alam, S.; Gorman-Lewis, D.; Chen, N.; Safari, S.; Baek, K.; Konhauser, K. O.; Alessi, D. S. Mechanisms of the Removal of U(VI) from Aqueous Solution Using Biochar: A Combined Spectroscopic and Modeling Approach. *Environ. Sci. Technol.* **2018**, *52* (22), 13057−13067.
(18) Hao, W.; Kashiwabara, T.; Jin, R.; Takahashi, Y.; Gingras, M.; Alessi, D. S.; Konhauser, K. O. Clay Minerals as a Source of Cadmium to Estuaries. *Sci. Rep.* **2020**, *10* (1), 10417.
(19) Ahmed, I. A. M.; Young, S. D.; Mosselmans, J. F. W.; Crout, N. M. J.; Bailey, E. H. Coordination of Cd2+ Ions in the Internal Pore System of Zeolite-X: A Combined EXAFS and Isotopic Exchange Study. *Geochim. Cosmochim. Acta* **2009**, *73* (6), 1577−1587.
(20) Logar, N. Z.; Šiljeg, M.; Arčon, I.; Meden, A.; Tušar, N. N.; Štefanović, Š. C.; Kovač, J.; Kaučič, V. Sorption of Cr3+ on Clinoptilolite Tuff: A Structural Investigation. *Microporous Mesoporous Mater.* **2006**, *93* (1−3), 275−284.
(21) Komárek, M.; Koretsky, C. M.; Stephen, K. J.; Alessi, D. S.; Chrastný, V. Competitive Adsorption of Cd(II), Cr(VI), and Pb(II) onto Nanomaghemite: A Spectroscopic and Modeling Approach. *Environ. Sci. Technol.* **2015**, *49* (21), 12851−12859.
(22) Li, X.; Pan, G.; Qin, Y.; Hu, T.; Wu, Z.; Xie, Y. EXAFS Studies on Adsorption-Desorption Reversibility at Manganese Oxide-Water Interfaces: II. Reversible Adsorption of Zinc on δ-MnO2. *J. Colloid Interface Sci.* **2004**, *271* (1), 35−40.
(23) Godelitsas, A.; Armbruster, T. HEU-Type Zeolites Modified by Transition Elements and Lead. *Microporous Mesoporous Mater.* **2003**, *61* (1−3), 3−24.
(24) Cerjan Stefanović, Š.; Zabukovec Logar, N.; Margeta, K.; Novak Tušar, N.; Arčon, I.; Maver, K.; Kovač, J.; Kaučič, V. Structural Investigation of Zn2+ Sorption on Clinoptilolite Tuff from the Vranjska Banja Deposit in Serbia. *Microporous Mesoporous Mater.* **2007**, *105* (3), 251−259.
(25) Ju, W. S.; Matsuoka, M.; Yamashita, H.; Anpo, M. Local Structure of Pb (II) Ion Catalysts Anchored within Zeolite Cavities and Their Photocatalytic Reactivity for the Elimination of N2O. *J. Synchrotron Radiat.* **2001**, *8* (2), 608−609.
(26) Bordiga, S.; Turnes Palomino, G.; Arduino, D.; Lamberti, C.; Zecchina, A.; Otero Areán, C. Well Defined Carbonyl Complexes in Ag+- and Cu+-Exchanged ZSM-5 Zeolite: A Comparison with Homogeneous Counterparts. *J. Mol. Catal. A: Chem.* **1999**, *146* (1−2), 97−106.
(27) Morra, E.; Berlier, G.; Borfecchia, E.; Bordiga, S.; Beato, P.; Chiesa, M. Electronic and Geometrical Structure of Zn+ Ions Stabilized in the Porous Structure of Zn-Loaded Zeolite H-ZSM-5: A Multifrequency CW and Pulse EPR Study. *J. Phys. Chem. C* **2017**, *121* (26), 14238−14245.
(28) Shao, D. D.; Fan, Q. H.; Li, J. X.; Niu, Z. W.; Wu, W. S.; Chen, Y. X.; Wang, X. K. Removal of Eu(III) from Aqueous Solution Using ZSM-5 Zeolite. *Microporous Mesoporous Mater.* **2009**, *123* (1−3), 1−9.
(29) Ouellet-Plamondon, C.; Lynch, R. J.; Al-Tabbaa, A. Comparison between Granular Pillared, Organo- and Inorgano-Organo-Bentonites for Hydrocarbon and Metal Ion Adsorption. *Appl. Clay Sci.* **2012**, *67−68*, 91−98.
(30) Zhang, Y.; Jin, F.; Shen, Z.; Lynch, R.; Al-Tabbaa, A. Kinetic and Equilibrium Modelling of MTBE (Methyl Tert-Butyl Ether) Adsorption on ZSM-5 Zeolite: Batch and Column Studies. *J. Hazard. Mater.* **2018**, *347*, 461−469.
(31) Zhang, Y. Characteristics and Mechanisms of Heavy Metal and MTBE Adsorption on Zeolites and Applications in Permeable Reactive Barriers. Ph.D. Dissertation, University of Cambridge, Cambridge, U.K., 2019. DOI: 10.17863/CAM.45900
(32) Hao, W.; Flynn, S. L.; Kashiwabara, T.; Alam, M. S.; Bandara, S.; Swaren, L.; Robbins, L. J.; Alessi, D. S.; Konhauser, K. O. The Impact of Ionic Strength on the Proton Reactivity of Clay Minerals. *Chem. Geol.* **2019**, *529*, 119294.
(33) Hao, W.; Flynn, S. L.; Alessi, D. S.; Konhauser, K. O. Change of the Point of Zero Net Proton Charge (PHPZNPC) of Clay Minerals with Ionic Strength. *Chem. Geol.* **2018**, *493*, 458−467.
(34) Indraratna, B.; Medawela, S. K.; Athuraliya, S.; Heitor, A.; Baral, P. Chemical Clogging of Granular Media under Acidic Groundwater Conditions. *Environ. Geotech.* **2019**, 1−13.
(35) Obiri-Nyarko, F.; Kwiatkowska-Malina, J.; Malina, G.; Wołowiec, K. Assessment of Zeolite and Compost-Zeolite Mixture as Permeable Reactive Materials for the Removal of Lead from a Model Acidic Groundwater. *J. Contam. Hydrol.* **2020**, *229*, 103597.
(36) Jiang, D. T.; Chen, N.; Sheng, W. Wiggler-Base Hard X-ray Spectroscopy Beamline at CLS. In *Synchrotron Radiation Instrumentation, Parts 1 and 2*; Choi, J. Y., Rah, S., Eds.; AIP Conference Proceedings; 2007; Vol. *879*, p 800.
(37) Tolkachev, S. S.; Stroganov, E. V.; Kozhina, I. I. The Structure of Lead Oxide Monohydrate. *Vestn. Leningr. Univ. Ser. Fiz. Khim* **1958**, *16*, 134−139.
(38) Rehr, J. J.; Albers, R. C. Theoretical Approaches to X-Ray Absorption Fine Structure. *Rev. Mod. Phys.* **2000**, *72* (3), 621−654.
(39) Ravel, B.; Newville, M. ATHENA, ARTEMIS, HEPHAESTUS: Data Analysis for X-Ray Absorption Spectroscopy Using IFEFFIT. *J. Synchrotron Radiat.* **2005**, *12*, 537−541.
(40) Ressler, T. WinXAS: A New Software Package Not Only for the Analysis of Energy-Dispersive XAS Data. *J. Phys. IV* **1997**, *7*, C2-269−C2-270.
(41) Joly, Y. X-Ray Absorption near-Edge Structure Calculations beyond the Muffin-Tin Approximation. *Phys. Rev. B: Condens. Matter Mater. Phys.* **2001**, *63* (12), 125120.
(42) Herbelin, A.; Westall, J. *FITEQL-A Computer Program for Determination of Chemical Equilibrium Constants from Experimental Data Version 3.2 User's Manual*; Corvallis, OR, 1996.
(43) Alessi, D. S.; Flynn, S. L.; Alam, M. S.; Robbins, L. J.; Konhauser, K. O. Potentiometric Titrations to Characterize the Reactivity of Geo-Microbial Surfaces. In *Analytical Geomicrobiology: A Handbook of Instrumental Techniques*; Cambridge University Press: Cambridge, U.K., 2019; pp 79−92.
(44) Karatas, M. Removal of Pb(II) from Water by Natural Zeolitic Tuff: Kinetics and Thermodynamics. *J. Hazard. Mater.* **2012**, *199−200*, 383−389.
(45) Zou, W.; Han, R.; Chen, Z.; Jinghua, Z.; Shi, J. Kinetic Study of Adsorption of Cu(II) and Pb(II) from Aqueous Solutions Using Manganese Oxide Coated Zeolite in Batch Mode. *Colloids Surf., A* **2006**, *279* (1−3), 238−246.
(46) Hui, K. S.; Chao, C. Y. H.; Kot, S. C. Removal of Mixed Heavy Metal Ions in Wastewater by Zeolite 4A and Residual Products from Recycled Coal Fly Ash. *J. Hazard. Mater.* **2005**, *127* (1−3), 89−101.
(47) Salem, A.; Akbari Sene, R. Removal of Lead from Solution by Combination of Natural Zeolite-Kaolin-Bentonite as a New Low-Cost Adsorbent. *Chem. Eng. J.* **2011**, *174*, 619.

(48) Ricordel, S.; Taha, S.; Cisse, I.; Dorange, G. Heavy Metals Removal by Adsorption onto Peanut Husks Carbon: Characterization, Kinetic Study and Modeling. *Sep. Purif. Technol.* **2001**, *24* (3), 389−401.
(49) Momčilović, M.; Purenović, M.; Bojić, A.; Zarubica, A.; Randelovic, M. Removal of Lead(II) Ions from Aqueous Solutions by Adsorption onto Pine Cone Activated Carbon. *Desalination* **2011**, *276* (1−3), 53−59.
(50) Oubagaranadin, J. U. K.; Murthy, Z. V. P. Adsorption of Divalent Lead on a Montmorillonite-Illite Type of Clay. *Ind. Eng. Chem. Res.* **2009**, *48* (23), 10627−10636.
(51) Lu, H.; Zhang, W.; Yang, Y.; Huang, X.; Wang, S.; Qiu, R. Relative Distribution of Pb2+ Sorption Mechanisms by Sludge-Derived Biochar. *Water Res.* **2012**, *46* (3), 854−862.
(52) Park, J. H.; Ok, Y. S.; Kim, S. H.; Cho, J. S.; Heo, J. S.; Delaune, R. D.; Seo, D. C. Competitive Adsorption of Heavy Metals onto Sesame Straw Biochar in Aqueous Solutions. *Chemosphere* **2016**, *142*, 77.
(53) Yakkala, K.; Yu, M. R.; Roh, H.; Yang, J. K.; Chang, Y. Y. Buffalo Weed (Ambrosia Trifida L. Var. Trifida) Biochar for Cadmium (II) and Lead (II) Adsorption in Single and Mixed System. *Desalin. Water Treat.* **2013**, *51* (40−42), 7732−7745.
(54) Wang, S.; Terdkiatburana, T.; Tadé, M. O. Adsorption of Cu(II), Pb(II) and Humic Acid on Natural Zeolite Tuff in Single and Binary Systems. *Sep. Purif. Technol.* **2008**, *62* (1), 64−70.
(55) Günay, A.; Arslankaya, E.; Tosun, İ. Lead Removal from Aqueous Solution by Natural and Pretreated Clinoptilolite: Adsorption Equilibrium and Kinetics. *J. Hazard. Mater.* **2007**, *146* (1), 362−371.
(56) Bektaş, N.; Kara, S. Removal of Lead from Aqueous Solutions by Natural Clinoptilolite: Equilibrium and Kinetic Studies. *Sep. Purif. Technol.* **2004**, *39* (3), 189−200.
(57) Wang, X.; Shao, D.; Hou, G.; Wang, X.; Alsaedi, A.; Ahmad, B. Uptake of Pb (II) and U (VI) Ions from Aqueous Solutions by the ZSM-5 Zeolite. *J. Mol. Liq.* **2015**, *207*, 338−342.
(58) Zhang, Y.; Jin, F.; Shen, Z.; Wang, F.; Lynch, R.; Al-Tabbaa, A. Adsorption of Methyl Tert-Butyl Ether (MTBE) onto ZSM-5 Zeolite: Fixed-Bed Column Tests, Breakthrough Curve Modelling and Regeneration. *Chemosphere* **2019**, *220*, 422−431.
(59) Zhanpeisov, N. U.; Ju, W. S.; Iino, K.; Matsuoka, M.; Anpo, M. Local Structure of Highly Dispersed Lead Species Incorporated within Zeolite: Experimental and Theoretical Studies. *Res. Chem. Intermed.* **2003**, *29* (4), 407−416.
(60) Um, W.; Papelis, C. Sorption Mechanisms of Sr and Pb on Zeolitized Tuffs from the Nevada Test Site as a Function of PH and Ionic Strength. *Am. Mineral.* **2003**, *88* (11−12), 2028−2039.
(61) Elzinga, E. J.; Sparks, D. L. X-Ray Absorption Spectroscopy Study of the Effects of PH and Ionic Strength on Pb(II) Sorption to Amorphous Silica. *Environ. Sci. Technol.* **2002**, *36*, 4352.


https://dx.doi.org/10.1021/acsestwater.0c00010
*ACS EST Water* 2021, 1, 108−116